



Boosting $2e^-$ oxygen reduction reaction in garland carbon nitride with carbon defects for high-efficient photocatalysis-self-Fenton degradation of 2,4-dichlorophenol

Yang Wu¹, Juan Chen¹, Huinan Che, Xin Gao, Yanhui Ao^{*}, Peifang Wang

Key Laboratory of Integrated Regulation and Resource Development on Shallow Lakes, Ministry of Education, College of Environment, Hohai University, No.1, Xikang Road, Nanjing 210098, China

ARTICLE INFO

Keywords:

Photocatalysis-self-Fenton system
Carbon defects
Oxygen reduction reaction
2,4-DCP degradation
DFT calculation

ABSTRACT

Photocatalytic two-electron oxygen reduction reaction ($2e^-$ ORR) has been regarded as a promising strategy to solve the disadvantage of Fenton technology (constant addition of H_2O_2). Herein, a photocatalysis-self-Fenton system was constructed on garland g- C_3N_4 with carbon defects (GCN-PSFs) for pollutants degradation. Carbon defects in the obtained GCN not only accelerate charge separation but also improve $2e^-$ ORR. As expected, the apparent rate constant for 2,4-DCP degradation by GCN-PSFs enhances to $0.070\ min^{-1}$, which is 5.4, 3.3 and 2.6 times as that of BCN, BCN-PSFs and GCN. The capture experiments and electron spin resonance indicate that the high activity is attributed to abundant $\cdot OH$ radicals, which are formed from the in-situ produced H_2O_2 . Density functional theory (DFT) calculation confirms that the carbon defects in GCN is favorable for photocatalytic $2e^-$ ORR to H_2O_2 . This work provides a new insight for high-efficient degradation of organic pollutants by PSFs.

1. Introduction

2,4-Dichlorophenol (2,4-DCP) with aromatic ring and chlorinated atoms, as a typical persistent organic pollutants (POPs), is a carcinogen and reluctant to be degraded by traditional chemical oxidation method or biological treatment technique [1–4]. Fortunately, advanced oxidation processes (AOPs) show excellent activity in degrading all kinds of organic pollutants [5–7]. Particularly, Fenton technology can generate abundant hydroxyl radicals ($\cdot OH$) with strong oxidation ability [8–11], which can degrade most of the refractory pollutants including aromatic compounds and some heterocyclic compounds in wastewater without selectivity [12]. However, there also exists a drawback that it needs to be constantly added with hydrogen peroxide (H_2O_2) in the whole reaction process, thus significantly limiting its practical application [13–16]. Noticeably, the method of generating and utilizing H_2O_2 in-situ in Fenton system can effectively avoid the cost consumption and safety risks caused by additional addition of H_2O_2 . Therefore, it is an urgent task to construct an in-situ self-Fenton system to efficiently remove 2,4-DCP from water environment.

Photocatalytic oxygen reduction reaction (ORR) has become a promising method for H_2O_2 production due to the advantages of safe

and efficient, environment-friendly and low cost [17–19]. Consequently, photocatalysis-self-Fenton system (PSFs) constructed by coupling photocatalysis [20–23] and Fenton technology may be an effective strategy for degradation of 2,4-DCP [24–26]. For instance, Zhang et al. designed a CdS/rGO/ Fe^{2+} PSFs, realizing the efficient degradation of various organic pollutants by using H_2O_2 in-situ generated over CdS [27]. Nevertheless, CdS has biological toxicity and instability, which greatly limits its application. Recently, graphite carbon nitride (g- C_3N_4) has been considered as a prospective ORR photocatalyst for H_2O_2 production owing to its high stability, appealing electronic structure and facile fabrication [28]. However, pure g- C_3N_4 still faces the inadequate utilization efficiency of light and rapid recombination of photogenerated charge carriers, resulting in poor photocatalytic H_2O_2 production activity [29]. To date, various strategies have been devoted to overcoming these drawbacks of g- C_3N_4 for improving photocatalytic H_2O_2 activity, such as morphology tuning [30], defect control [31], loading noble metal nanoparticles [32], elemental doping [33] and coupling with other semiconductors etc. [34]. Among above strategies, morphology and defect control can not only enhance light harvesting and ORR ability, but also facilitate the charge migration and separation [35–37]. Hence, morphology and defect regulation are regarded as prospective

^{*} Corresponding author.

E-mail address: andyao@hhu.edu.cn (Y. Ao).

¹ The two authors contribute equally to the work.

strategies for the construction PSFs to enhance the photocatalytic degradation performance of 2,4-DCP.

In this work, different morphologies g-C₃N₄-PSFs were constructed using melamine as precursor. The obtained garland g-C₃N₄ (GCN) with carbon defects not only shows fast separation of charge carriers but also exhibits higher ORR capability. As expected, the GCN possesses the highest photocatalytic H₂O₂ production activity (507.82 $\mu\text{M h}^{-1} \text{g}^{-1}$) in pure water, which is 6.8 times as that of bulk g-C₃N₄ (BCN). Correspondingly, GCN-PSFs shows the highest apparent rate constant (k_{app}) value of 0.07 min^{-1} , which is about 5.4 times as that of BCN ($k_{app} = 0.013 \text{ min}^{-1}$). Photoluminescence spectroscopy (PL), photocurrent response (PCR) and electrochemical impedance spectra (EIS) proved that the GCN with carbon defects possesses high separation effectivity of charge carriers. Capture experiments and electron spin resonance (ESR) analyses verified that excellent degradation activity was attributed to the abundant $\cdot\text{OH}$ radicals, which was on account of efficient utilization of in-situ produced H₂O₂. And the density functional theory (DFT) calculations results indicated that GCN with carbon defects was more conducive to adsorbing O₂, which facilitated the 2e⁻ ORR to form H₂O₂. Generally, the PSFs over morphology and defect modification in this work provides a new vision and strategy for degrading organic contaminants.

2. Experimental sections

2.1. Synthesis of four different morphologies of g-C₃N₄

2.1.1. Preparation of bulk g-C₃N₄ (BCN)

BCN was prepared by thermal treatment of melamine. Specifically, 2.0 g melamine utilized as precursor was placed into a porcelain boat and then put in the muffle furnace at 550 °C for 4 h with a ramping rate of 2.3 °C/min.

2.1.2. Preparation of ultrathin g-C₃N₄ (UCN)

UCN was prepared by the second thermal polymerizing of BCN. In detail, 2.0 g BCN was put into the porcelain and then placed into the muffle furnace at 500 °C for 4 h with a ramping rate of 2.3 °C/min.

2.1.3. Preparation of tubular g-C₃N₄ (TCN)

1.0 g of melamine was added into 60 mL of deionized (DI) water at 90 °C under vigorous stirring in a thermostatic oil bath until it was completely dissolved in the water. Followed by a watery liquid was obtained, and subsequently transferred into a Teflon-lined stainless-steel autoclave. The hydrothermal reaction was carried out at 180 °C for 24 h.

A kind of sediment was achieved, and then it was separated by using a centrifuge. The resulting solid was washed with DI water for 3 times before dried at 60 °C under vacuum condition. Ultimately, the obtained product placed into a porcelain boat was calcined at 550 °C for 4 h with a ramping rate of 2.3 °C/min under nitrogen (N₂) atmosphere.

2.1.4. Preparation of garland g-C₃N₄ (GCN) with carbon defects

0.5 g of melamine was completely dissolved in 30 mL dimethyl sulfoxide (DMSO) and it was denoted as A. 0.51 g cyanuric acid was totally dissolved in another 30 mL DMSO solution denoted as B. Then, the solution B was dropped into solution A at a constant rate. A milky white precipitate was obtained. Then the mixture was stirred for 30 min. Subsequently, 0.1 g oxalic acid was added into the mixture under stirring for 30 min. The resulting mixture was obtained by centrifugation and then washed more than 6 times with DI water and ethanol. Finally, the obtained product placed into a porcelain boat was calcined at 550 °C for 4 h with a ramping rate of 2.3 °C/min under N₂ atmosphere. And the general synthesis process of four different morphologies g-C₃N₄ (BCN, UCN, TCN and GCN) are displayed in Fig. 1.

2.2. Characterization

The scanning electron microscopy (SEM; S-4800, Hitachi, Japan) and transmission electron microscope (TEM; JEM-F200, JEOL, Japan) were carried out to characterize the microscopic morphology and structure of the g-C₃N₄ in this work. The crystalline of as-prepared catalysts was revealed through the powder X-ray diffraction (XRD; Rigaku, Japan). What's more, in order to further reveal the chemical structure of catalysts, the X-ray photoelectron spectroscopy (XPS; Thermo Scientific K-Alpha⁺, USA) and Fourier-transform infrared spectroscopy (FTIR; Tensor 27, Bruker Optics, German) were performed. The UV-vis diffuse reflectance spectra (DRS) was gained by using the UV-Vis spectrophotometer (UV-3600, Shimadzu, Japan) with a reflectance standard BaSO₄ powder. The photoluminescence spectroscopy (PL) with 370 nm excitation wavelength and the three-dimensional excitation-emission matrix fluorescence spectra (3D EEMs) were performed on fluorescence spectrometer (F-7000, Hitachi, Japan). The Electron spin resonance (ESR) was performed in Bruker ESR JESFA200 spectrometer. The general prepared process was as follows: 5,5-dimethyl-1-pyrroline N-oxide (DMPO) was used as a spin capture agent. Firstly, 1 mg/mL of the catalyst was prepared with DI water as the solvent and then ultrasound for 5 min. Took 30 μL uniformly dispersed solution and added 30 μL DMPO (100 mM) into it. Finally, the resulting solution was expected to be analyzed.

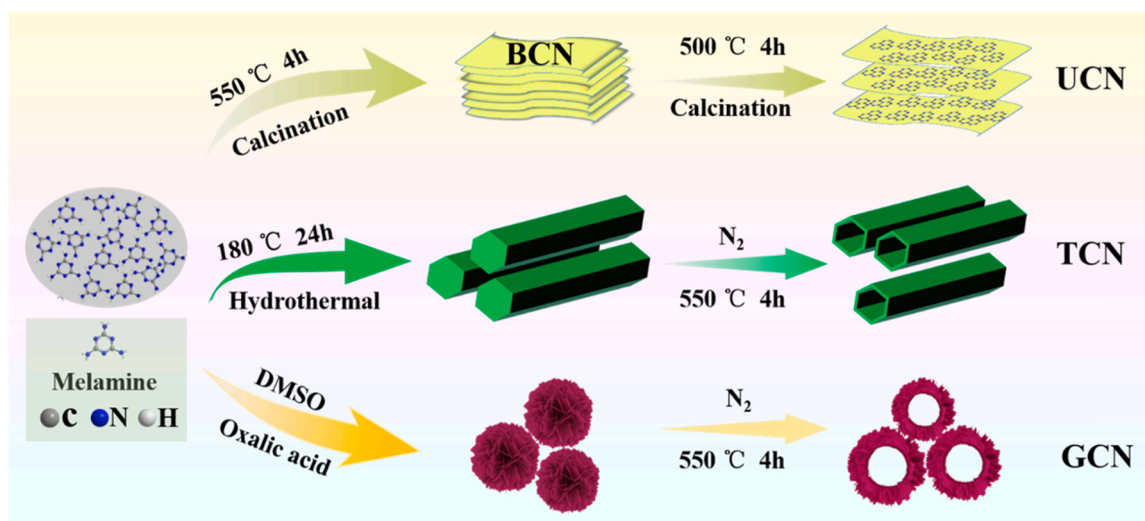


Fig. 1. Synthesis schematic diagram of g-C₃N₄ with four different morphologies (BCN, UCN, TCN and GCN).

2.3. Photoelectrochemical performance measurement

The photoelectrochemical properties including photocurrent response (PCR), Mott-Schottky plot and electrochemical impedance spectra (EIS) were measured on the electrochemical workstation (CHI660D, Chenhua, China) with standard three electrodes. The Ag/AgCl electrode and Pt foil are regarded as the reference electrode and counter-electrode, respectively. The sample preparation process was as follows: 40 mg as-prepared sample was mixed with 500 μ L ethanol, 500 μ L ethylene glycol and 100 μ L Nafion in 2 mL centrifuge tube, and then ultrasonized until it was well mixed. Then, 100 μ L of the evenly mixed sample was uniformly spread onto the conductive surface of indium tin oxide (ITO) glass, with an area of 1 cm^2 . What particularly worth mentioning is that the photocurrent response (PCR) and Mott-Schottky plot were investigated in 0.5 M Na_2SO_4 aqueous solution while the electrochemical impedance spectra (EIS) was carried out in 0.1 M KCl solution containing 5 mM $[\text{Fe}(\text{CN})_6]^{3-}/[\text{Fe}(\text{CN})_6]^{4-}$ solution, respectively.

Similarly, the Rotating disk electrode (RDE) was operated on a Chenhua CHI 760E electrochemical workstation equipped with standard three electrodes. The function of the three electrodes is similar to the above, but there are some differences in the preparation of the working electrode. The general preparation process of the working electrode is as follows: 5 mg of catalysts were evenly dispersed in 1 mL of ethanol solution containing 100 μ L Nafion by continuous ultrasound treatment. 5 mL of the prepared sample was evenly applied to a clean glassy carbon electrode and air-dried at room temperature. The linear sweep voltammetry (LSV) was investigated in a phosphate buffer solution with pH = 7 and oxygen saturated condition. The LSV curves was obtained under the scan rate of 5 mV s^{-1} and the rotating speeds are 400 rpm, 800 rpm, 1200 rpm, 1600 rpm and 2500 rpm, respectively. The number of electrons (n) involved in the reaction during oxygen reduction can be fitted by the following formula (1) and (2) [38]:

$$j^{-1} = j_k^{-1} + B^{-1} \omega^{-1/2} \quad (1)$$

$$B = 0.2nFC_0D_0^{2/3}\nu^{-1/6} \quad (2)$$

where j , j_k and ω represent the measured current density, kinetic current density and rotating speed (rpm), respectively. F is the Faraday constant (96,485 C mol^{-1}). What's more, ν is the kinetic viscosity of water (0.01 $\text{cm}^2 \text{s}^{-1}$). C_0 and D_0 are the bulk concentration of O_2 in water ($1.1 \times 10^{-3} \text{ mol cm}^{-3}$) and diffusion coefficient of O_2 ($1.93 \times 10^{-5} \text{ cm}^2 \text{s}^{-1}$), respectively.

2.4. Photocatalytic activity of H_2O_2 generation

The photocatalytic activity evaluation was performed under visible light with 700 mW/cm^2 Xenon lamp ($\lambda > 420 \text{ nm}$) and the experimental temperature was controlled at 25 $^\circ\text{C}$ through a condensing device. The concentration of H_2O_2 was determined by a UV-visible spectrophotometer [39]. In general, 25 mg of the catalysts were put into 50 mL of water containing 10 vol% isopropanol (IPA) solution in a beaker and ultrasonic dissolution for 5 min. Then, under the condition of avoiding light, the solution was uniformly oxygenated for 30 min and constantly stirred. Adjusting the distance between the light source and the beaker and kept it fixed. The lamp should be preheated for 30 min before the photocatalytic reaction was triggered. During the whole reaction, 1.5 mL of the resulting solution was transferred to centrifuge tube at regular intervals and centrifuged to remove the sediment. Subsequently, under the action of Horseradish Peroxidase (HRP) and N, N-diethyl-p-phenylenediamine sulfate (DPD), the supernatant develops color reaction and then taken to measure the concentration of H_2O_2 with absorption peak at 551 nm.

2.5. The test of 2,4-DCP degradation activity in PSFs

The efficiency of the degradation of the 2,4-DCP was measured by high performance liquid chromatography (HPLC). The mobile phases consisted of methyl alcohol and water with a volume ratio of 80:20. What's more, the flow rate, injection volume and testing cycle are 1 mL/min, 10 μ L and 4 min, respectively. The experiment was performed in a beaker with 25 mg of the catalyst and 50 mL 2,4-DCP solution (5 ppm) and ultrasonic dissolution for 5 min. The obtained solution was oxygenated constantly for 30 min under dark condition. The $\lambda > 420 \text{ nm}$ visible-light lamp used as a light source to trigger the reaction should be preheated. At this moment, 5 mg $\text{FeSO}_4 \cdot 7\text{H}_2\text{O}$ was put into the resulting solution. The light was turned on shining directly on the solution to excite PSFs to degrade the contaminant. The degradation process lasted for 30 min and 1.5 mL of solution in the reaction was sucked into the centrifuge tube and centrifuged every 5 min. The upper clarification fluid is measured. In addition, the argon (Ar), isopropanol (IPA) and triethanolamine (TEOA) were used to scavenge superoxide radicals ($\cdot\text{O}_2^-$), hydroxyl radicals ($\cdot\text{OH}$) and holes (h^+) in the 2,4-DCP degradation process, respectively. Moreover, the Langmuir-Hinshelwood equation [40] and calculation formula of free radical contribution rate (R) are as follows [41]:

$$\ln(C_0/C_t) = K_{app}t \quad (3)$$

$$\frac{R \cdot \text{OH}}{K_{app}} = \frac{K_{\cdot\text{OH}}}{K_{app}} \approx (K_{app} - K_{\text{IPA}}) \quad (4)$$

$$\frac{R \cdot \text{O}_2^-}{K_{app}} = \frac{K_{\cdot\text{O}_2^-}}{K_{app}} \approx (K_{app} - K_{\text{Ar}}) \quad (5)$$

$$\frac{R h^+}{K_{app}} = \frac{K_{h^+}}{K_{app}} \approx (K_{app} - K_{\text{TEOA}}) \quad (6)$$

where C and C_0 are the concentration of 2,4-DCP at time t and initial time. And k_{app} is the apparent rate constant. Moreover, k_{IPA} , k_{Ar} and k_{TEOA} are the apparent rate constant in the presence of the corresponding radical scavengers during 2,4-DCP degradation process. Other types of pollutants including sulfamethoxazole (20 ppm), 4-acetamidophenol (20 ppm), imidacloprid (10 ppm) and acetamiprid (20 ppm) were used as target contaminants. Similarly, 25 mg catalyst was added to 50 mL degradation solution and the degradation process is similar to that of 2,4-DCP in other details.

2.6. DFT calculation

The density functional theory (DFT) performed with Gaussian 16 C.01 [42] and ORCA 4.2.1 [43] software package is used to further find out where the contaminant molecules are more easily attacked and adsorption energy (E_{ads}) of O_2 . The highest occupied molecular orbital (HOMO), the lowest unoccupied molecular orbital (LUMO) and the surface electrostatic potential (ESP) calculated on Multiwfn 3.8 (dev) [44] drawn with VMD (1.9.3 version) [45] are used to reveal the regions at which pollutant molecules are vulnerable to attack. Finally, f^0 (radical attack), f^- (electrophilic attack) and f^+ (nucleophilic attack) and CDD (condensed dual descriptor) obtained by Fukui index are applied to analyze the sites theoretically most vulnerable for radical, electrophilic, nucleophilic species attack and comprehensive vulnerable sites, respectively. More details on DFT calculation can be found in Text S1 of the [Supplementary data](#).

3. Results and discussion

3.1. Characterizations

Fig. 2 shows the morphologies of as-synthesized catalysts by SEM and TEM images. Notably, the precursor of four kinds of g-C₃N₄ is all melamine, but they show different morphological characteristics under diverse treatment methods. From Fig. 2a and e, BCN appears as a typical large blocky structure, presenting compact monolith-like morphology. After the secondary calcination, the massive BCN was peeled off into many nanosheets, which were stacked together due to van der Waals forces to obtain UCN (Fig. 2b and f). It can be seen from Fig. 2c and inserted diagram that the TCN is a standard hexagon stereoscopic tube nanotube length whose length can be up to 200 μm , and correspondingly the diameter varies from 20 to 70 μm (Fig. 2g). Interestingly, Fig. 2d shows a flower cluster composed of multiple GCN which looks like beautiful flowers with a number of jagged petals. Fig. 2h and Fig. 2i display a more elaborate description about the garland GCN with the diameter of 1.2 μm . The irregular arrangement of nanosheets was stacked into flower spheres, and then the hollow was formed in the middle of the wreath under the action of oxalic acid to obtain the flower-ring GCN. A more detailed TEM images of the BCN UCN, TCN and GCN are shown in the Fig. S1.

As shown in Fig. 3a, all the samples show similar peaks in the X-ray diffraction (XRD), indicating that similar crystalline structures existed in them. Particularly, there exists two distinct diffraction peaks at 12.9°

(100) and 27.8° (002) owing to the ordered arrangement of tri-s-triazine in-plane and the interlayer stacking of conjugated aromatic system of g-C₃N₄ as expected [46]. What's more, the diffraction peak at (002) crystal facet of TCN and GCN are more weaker and broader compared with that of BCN and UCN, illustrating that there existed less crystallinity in TCN and GCN [47]. Additionally, in order to further explore the microstructure of the as-prepared catalysts, the FTIR spectra were performed and shown in Fig. 3b. It is clear that the FTIR spectra of the four catalysts are semblable, indicating that morphology change has little influence on chemical structure. Respectively, the distinct peaks at 810 cm^{-1} , 1200–1600 cm^{-1} and 3000–3600 cm^{-1} are attributed to the existence of triazine unit, aromatic C-N heterocyclic units and the stretching vibrations of OH/NH₂ [48]. The XPS was also carried out to further verify the composition of as-prepared catalysts. From Fig. S2, all characteristic peaks of constituent elements in the corresponding catalysts can be clearly observed including C, N and O. Obviously, there exists two evident characteristic peaks at 284.46 eV and 287.92 eV in C 1s (Fig. 3c) due to the presence of sp² C-C/C=C bonds and sp² N=C-N bonds, respectively [49]. In high resolution N 1s spectra (Fig. 3d), there are three peaks at 398 eV, 399 eV and 400 eV severally assigned to the existence of CN=C, N-[C]₃ and C-NH_x [50]. Additionally, the atomic content of C and N over catalysts were also measured by XPS. Obviously, as illustrated in the Fig. 3e, the C/N ratio is from 0.98 for BCN to 0.78 for GCN, preliminarily revealing the introduction of carbon defects on the surface of GCN [51]. To further prove the existence of carbon defects, the EPR spectra was performed shown in Fig. 3f. GCN with carbon

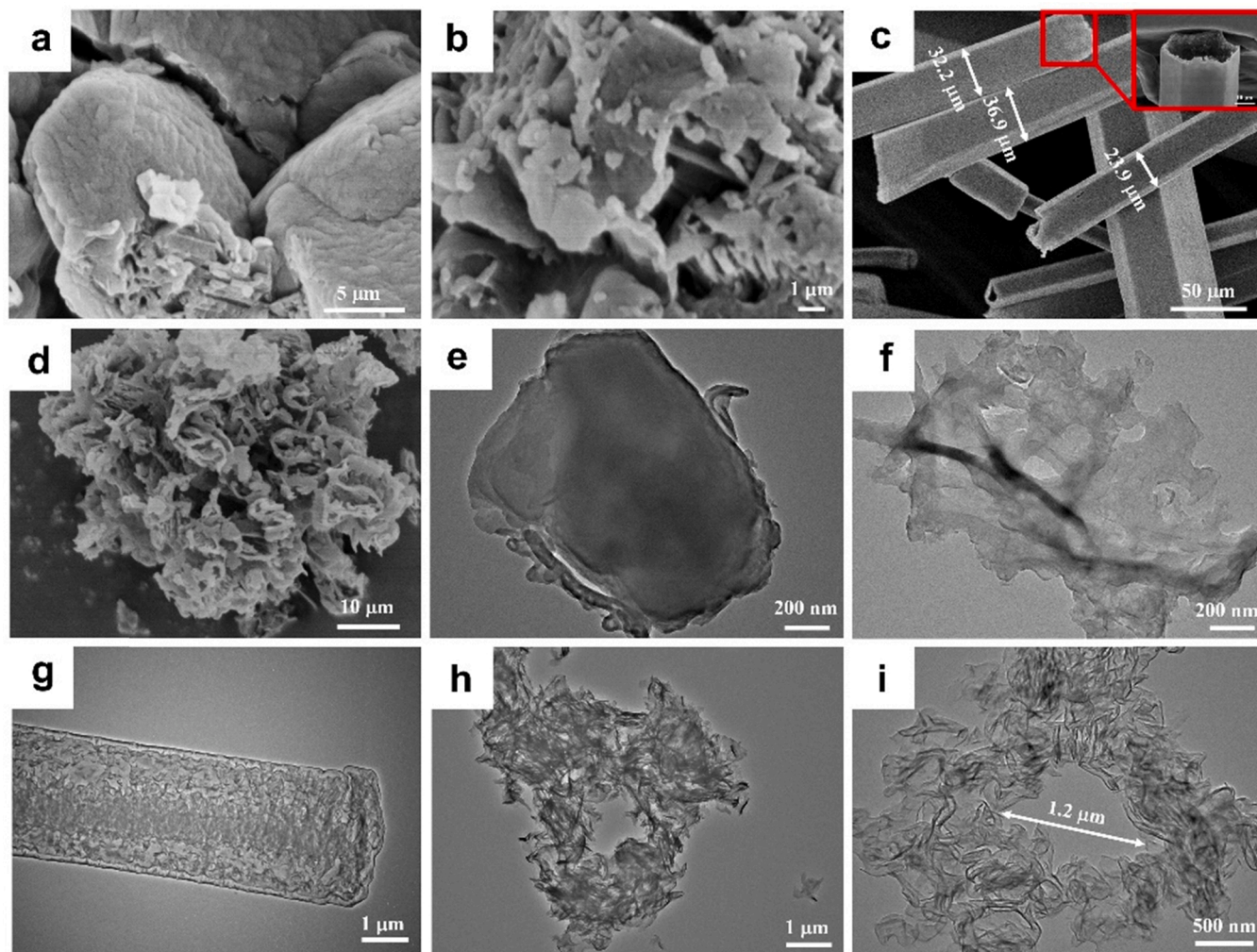


Fig. 2. (a–d) SEM images and (e–h) TEM images of BCN, UCN, TCN and GCN. (i) Enlarged TEM images of GCN.

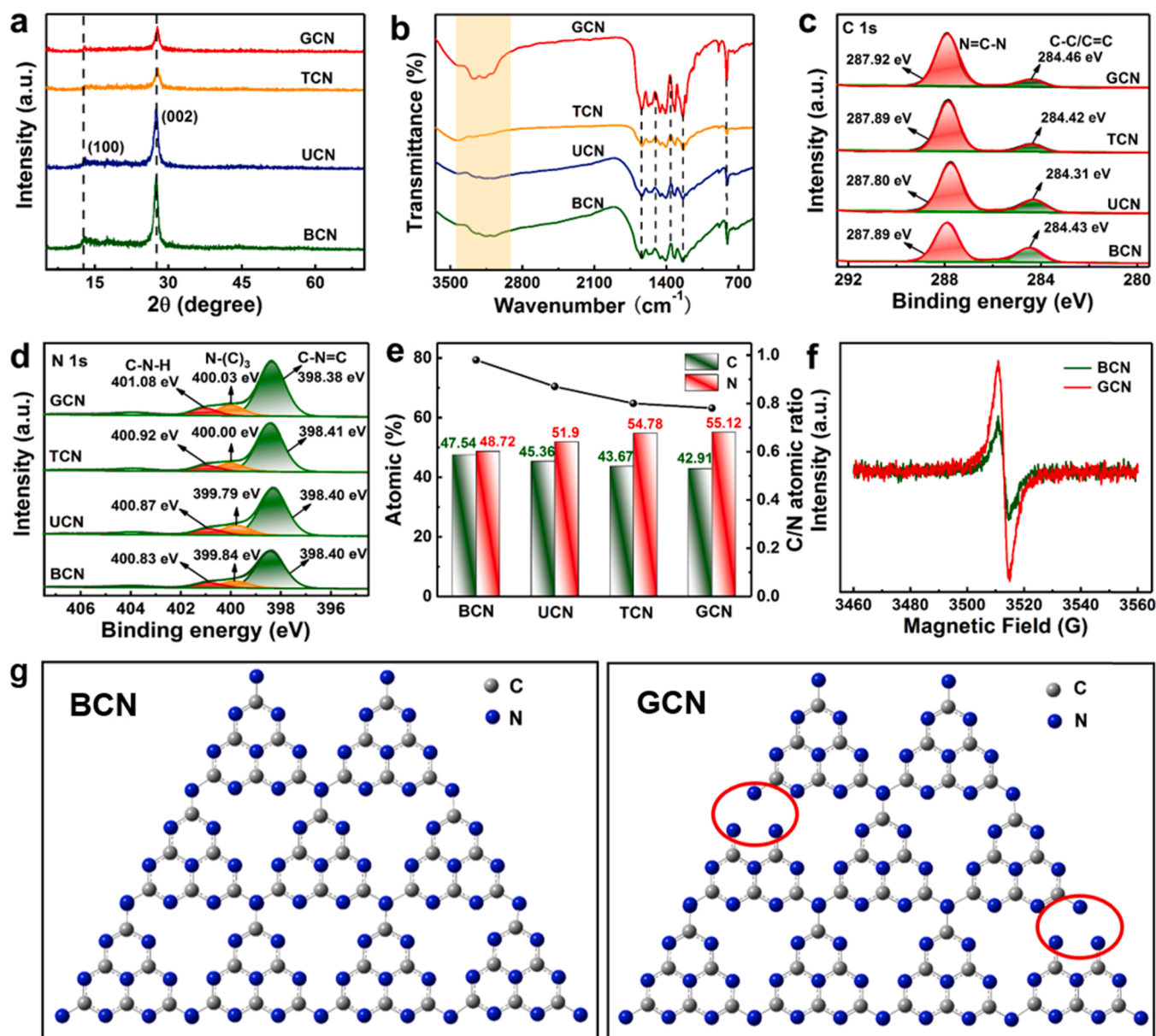


Fig. 3. (a) XRD patterns and (b) FTIR spectra of BCN, UCN, TCN and GCN. (c) C 1s and (d) N 1s of BCN, UCN, TCN and GCN. (e) C and N atom content and C/N atomic rate of as-prepared samples. (f) EPR spectra of BCN and GCN. (g) Schematic structure of (a) BCN and (b) GCN with C-defects.

defects presents a stronger EPR signal peak relative to BCN which is due to the presence of more unpaired electrons generating from carbon defects. From the C/N ratio and EPR analysis, a conclusion could be drawn that a large number of carbon defects are introduced in the formation of GCN. The possible schematic structures of BCN and GCN are displayed in Fig. 3g.

3.2. Photocatalytic H_2O_2 production and PSFs degradation

The photocatalytic H_2O_2 production and degradation activity of as-synthesized samples were evaluated under visible light (300 W Xe lamp, $\lambda > 420$ nm). As shown in Fig. 4a and b, BCN shows the lowest photocatalytic H_2O_2 production activity ($4.31 \text{ mM h}^{-1} \text{ g}^{-1}$), which may be due to fewer reactive sites and low carrier separation efficiency. Nevertheless, compared to BCN, the photocatalytic performance on H_2O_2 production for UCN ($5.92 \text{ mM h}^{-1} \text{ g}^{-1}$) and TCN ($8.11 \text{ mM h}^{-1} \text{ g}^{-1}$) is significantly enhanced. Especially, GCN exhibits the highest photocatalytic activity for H_2O_2 production ($21.59 \text{ mM h}^{-1} \text{ g}^{-1}$), which

is about 5 times than that of BCN. This phenomenon is mainly caused by that the garland-like ring structure and carbon defects endow GCN with highest charge separation efficiency. What's more, the corresponding absorbance diagrams of all as-prepared samples are illustrated in Fig. S3. Furthermore, the results of control experiment illustrated that H_2O_2 production is a photocatalytic reaction process (Fig. S4). In addition, the formation rate constant (k_f) of GCN reaches up to a maximum ($14.65 \text{ } \mu\text{M min}^{-1}$), which is about 7.08, 4.77, 3.31 times as that of BCN, UCN and TCN, while the decomposition rate constant (k_d) of all samples are almost equivalent, illustrating that H_2O_2 generated over GCN owns good stability (Fig. S5). Consequently, based on the excellent H_2O_2 production of GCN, we attempted to establish the PSFs without the addition of IPA on the basis of morphology exploration. In Fig. 4c and Fig. S6, GCN ($507.82 \text{ } \mu\text{M h}^{-1} \text{ g}^{-1}$) still displays higher photocatalytic performance of H_2O_2 production than that of BCN ($74.56 \text{ } \mu\text{M h}^{-1} \text{ g}^{-1}$) in the absence of IPA. For comparison, we found that the 2,4-DCP degradation activity of BCN and GCN is only 32.4% and 55.5% in the sole photocatalytic degradation system (Fig. 4d). Conversely, when Fe^{2+} was

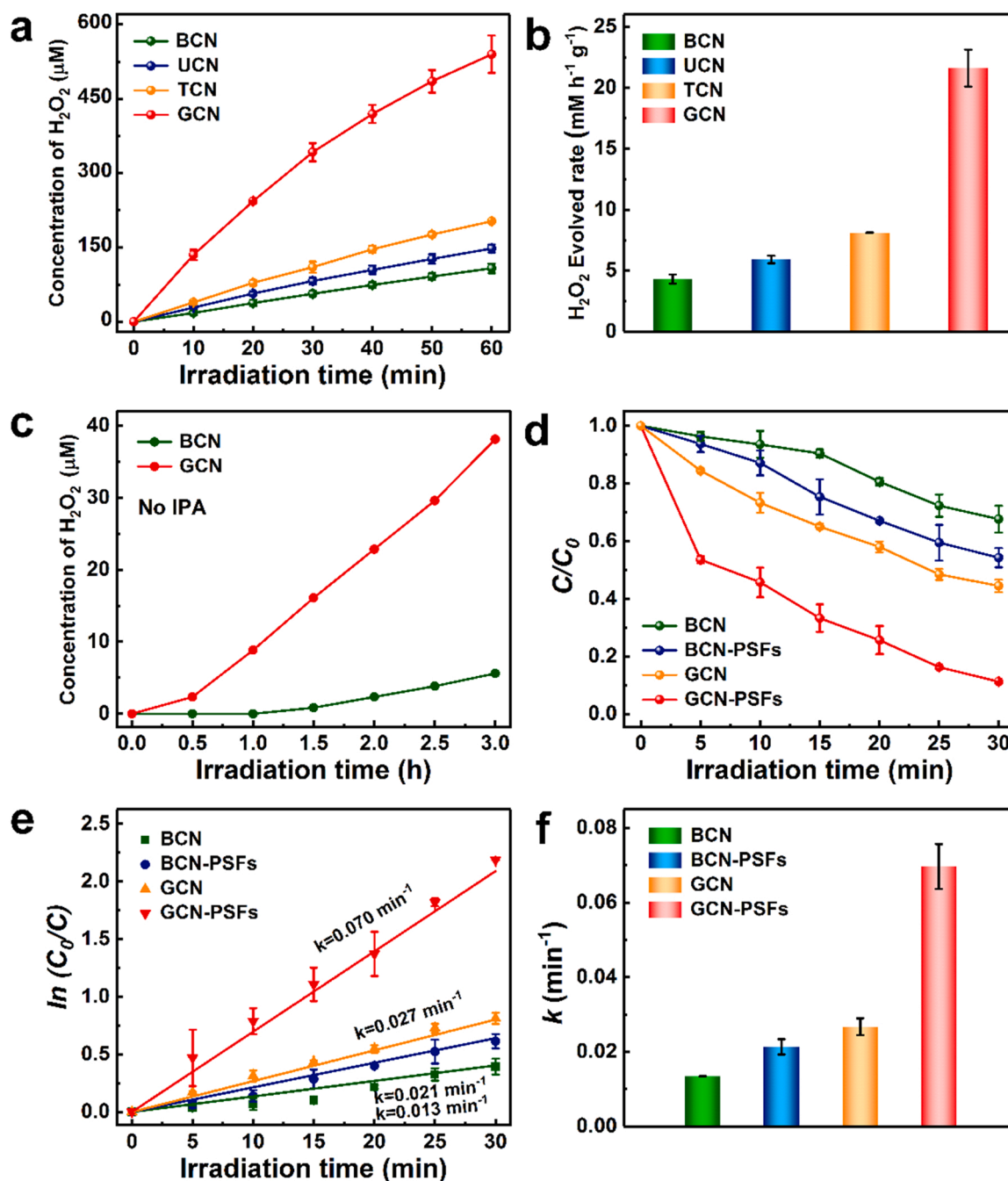


Fig. 4. (a) Photocatalytic H_2O_2 production of BCN, UCN, TCN and GCN with IPA under visible light irradiation. (b) Time courses of H_2O_2 evolved rate with IPA. (c) Photocatalytic H_2O_2 production of BCN and GCN without IPA under visible light irradiation. (d) The photocatalytic decomposition curves of 2,4-DCP with BCN, BCN-PSFs, GCN and GCN-PSFs under visible light irradiation. (e) The first-order reaction kinetic constants and (f) Bar chart of 2,4-DCP degradation.

added to the photocatalytic degradation system to form the PSFs, the degradation performance of both BCN and GCN is reaching up to 45.8% and 88.8%, respectively. Most importantly, k_{app} value of PSFs for GCN enhances as high as $0.070 min^{-1}$, which is 5.4, 3.3 and 2.6 times as than that of photocatalysis over BCN, BCN-PSFs and GCN (Fig. 4e and f). Hence, compared with single photocatalytic degradation, satisfactory degradation efficiency was demonstrated over PSFs, which may be originated from more active species with strong oxidation were generated, so as to efficiently degrade pollutants.

To verify the contribution of different free radicals in the degradation of 2,4-DCP for GCN-PSFs, quench experiments were carried out. The agents of argon (Ar), isopropanol (IPA) and triethanolamine (TEOA) are responsible for scavenging superoxide radical ($\cdot O_2^-$), hydroxyl radical

($\cdot OH$) and holes (h^+) in the 2,4-DCP degradation process, respectively. As shown in Fig. 5a and b, the degradation efficiency of 2,4-DCP decreased mildly under the condition of bubbling Ar through the whole experimental process, indicating that $\cdot O_2^-$ is not the main active species. It should be noted that when IPA and TEOA were added to the reaction system, the degradation rate was significantly inhibited by 58.0% and 44.9%, illustrating that $\cdot OH$ and h^+ were responsible for the decomposition of 2,4-DCP and $\cdot OH$ played the leading role. To clearly verify the contribution of different active species, the contribution rate was calculated. Apparently, $\cdot OH$ possesses the highest contribution rate (80.3%), and outperforms the $\cdot O_2^-$ and h^+ , indicating that the construction of GCN-PSFs can produce more $\cdot OH$ to degrade 2,4-DCP (Fig. 5b). Additionally, the presence of $\cdot OH$ and $\cdot O_2^-$ in the GCN-PSFs

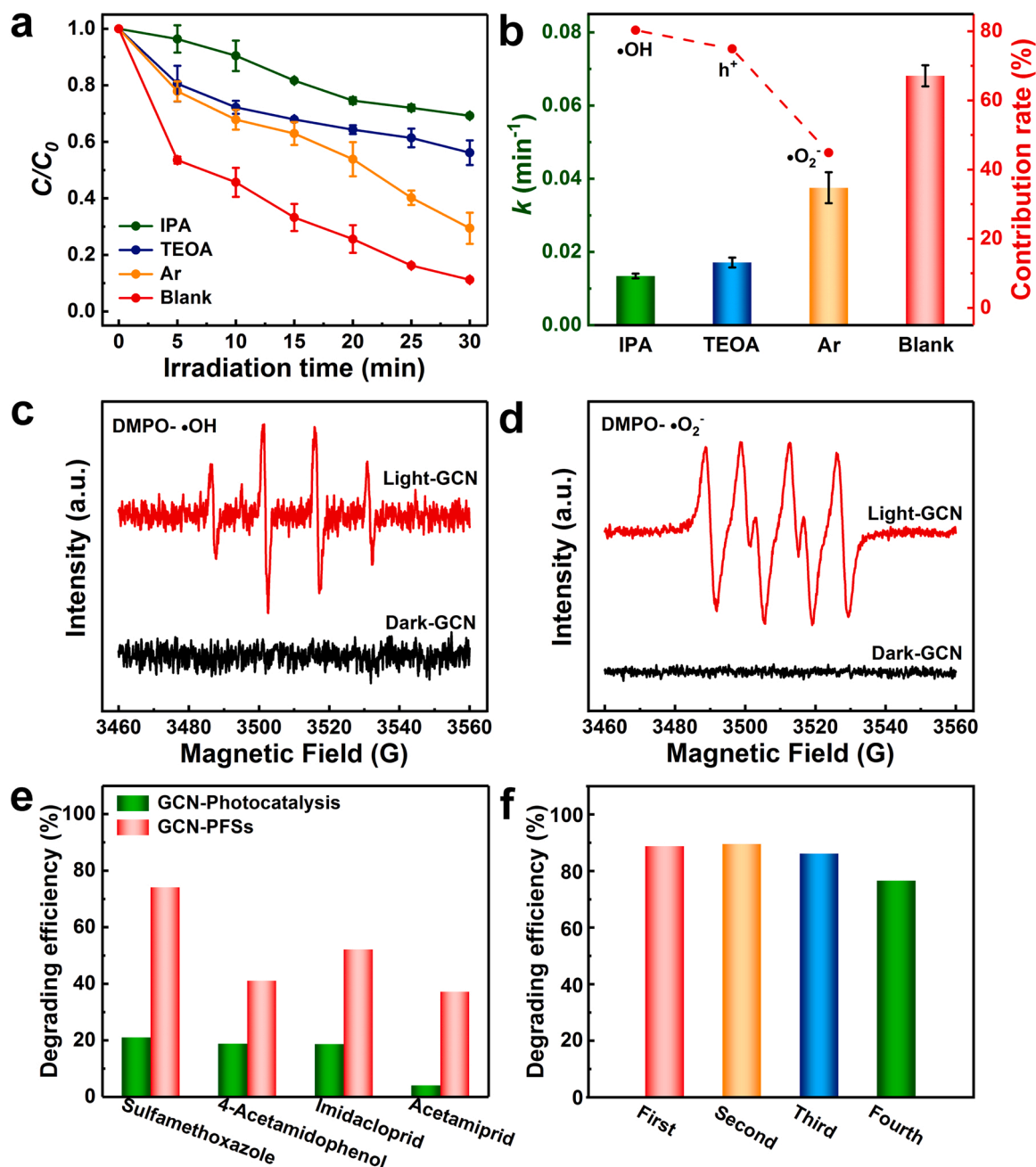


Fig. 5. (a) The decomposition curves of 2,4-DCP on GCN-PSFs with different radical scavengers. (b) The first-order reaction kinetic constants and free radical contribution of 2,4-DCP degradation on GCN-PSFs. ESR spectra of the (c) DMPO-•OH and (d) DMPO-•O₂[•] adducts on GCN under different conditions. (e) Degradation activity to other pollutants over GCN-PSFs. (f) Study on the stability of GCN-PSFs in degrading 2,4-DCP.

can be further proven by ESR spectra shown in Fig. 5c and d. Moreover, to prove the universality of the formed GCN-PSFs, other types of pollutants were used as target contaminants. As expected, the GCN-PSFs over all the four pollutants exhibit excellent degradation property (Fig. 5e). As for the stability of the catalyst itself, the degradation performance of GCN is maintained in a stable state after four cycles of testing under the same conditions (Fig. 5f) and no obvious changes have taken place in XRD patterns and FTIR spectra after circulation (Fig. S7).

3.3. DFT calculations and possible degradation pathways

The chemical properties of substances are determined by their structure. Especially, functional groups play a decisive role in the properties of organic substances. As displayed in Figs. 6a, 2,4-DCP is

composed of one phenyl, one hydroxyl and two chlorine atoms. To further accurately locate the reaction regions of 2,4-DCP, DFT calculation was carried out. As shown in Fig. 6b and c, the HOMO orbit of 2,4-DCP mainly located on the O10, C113, and C6 region, while the LUMO orbit of 2,4-DCP mainly located on the benzene ring region [52]. These sites are susceptible to be attacked by active substances during pollutant degradation process. What's more, the ESP was calculated to illustrate the density of the electron cloud on the pollutant surface as shown in Fig. 6d. It's worth noting that the electrons are mainly focused on C112 and C113, indicating that the deelectrification reaction occurs mainly at this position.

Based on the above analysis of molecular orbital and ESP, the regions that are prone to react in pollutant molecules are initially located. However, to further locate the atoms, which is more susceptible to be

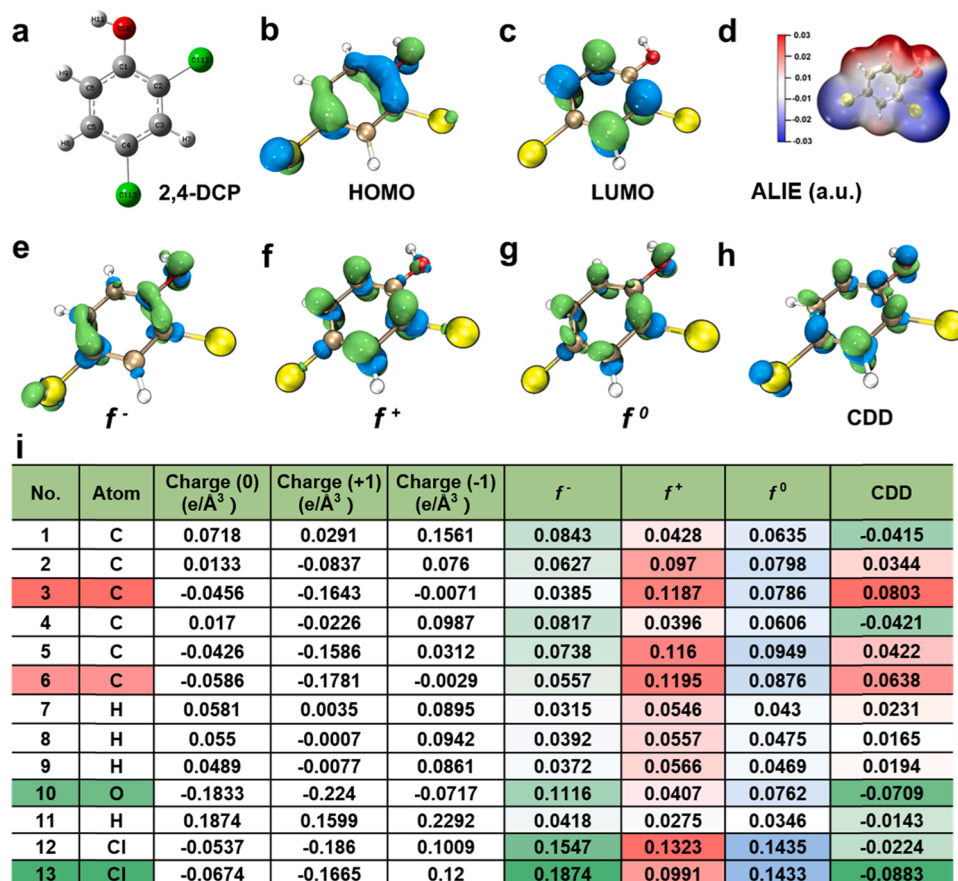


Fig. 6. (a) Optimized molecular structure, (b) HOMO orbital, (c) LUMO orbital and (d) ESP of 2,4-DCP. The isosurface of (e) f^- , (f) f^+ , (g) f^0 and (h) CDD of 2,4-DCP. (i) Natural population analysis (NPA) charges and calculated Fukui index results of 2,4-DCP.

attacked, the Hirshfeld charges and Fukui index (f^0 , f^- , f^+ and CDD) were calculated. The computed structure of f^- , f^+ , f^0 displayed in Fig. 6e–g. Theoretically speaking, in the contaminant structure, the f^0 , f^- , f^+ values of atoms are proportional to the potential for radical, electrophilic and nucleophilic species attack occurrence, respectively [53]. In common active species, $\cdot\text{O}_2^-$ and h^+ are respectively considered as nucleophilic species and electrophilic species, while $\cdot\text{OH}$ is treated as not only nucleophilic species but also free radical philophiles. It can be concluded from previous capture experiments that it is $\cdot\text{OH}$ and h^+ that play a main role in GCN-PSFs. When some atoms are equipped with both nucleophilic and electrophilic, we can use the value of CDD to comprehensively consider the potential of an atom to react when attacked by an active substance (Fig. 6h). The intuitive isosurface image of the Fukui function and specific calculation results are exhibited in Fig. 6i. C3, C6, O10 and Cl13 are theoretically considered as the most active locations.

The HPLC-MS was performed to reveal the main intermediates produced in the degradation process of 2,4-DCP. Combined with above DFT calculation results, two degradation pathways can be speculated during the degradation of 2,4-DCP in GCN-PSFs and GCN without Fe^{2+} shown in Fig. 7a and Fig. S8a. The Cl13 with the highest CDD value tends to be attacked by $\cdot\text{OH}$ and h^+ to produce R1 ($m/z = 131$). Due to the comparatively high CDD value of O10 (-0.0709), the R1 ($m/z = 131$) gives birth to R2 ($m/z = 218$) under the attack of $\cdot\text{O}_2^-$ and h^+ . R2 is then degraded into R3 ($m/z = 171$), which is eventually converted to smaller and less toxic molecules. In addition, there exists another pathway in the system. The Cl13 is also susceptible to obtain hydroxyl groups by stripping chlorine atom under the attack of $\cdot\text{OH}$ alone. The R4 ($m/z = 141$) reacts with $\cdot\text{OH}$ and h^+ further to form two isomers which are R5 ($m/z = 111$) or R6 ($m/z = 111$). R5 further gets rid of a dehydroxyl

groups to form R7 ($m/z = 97$). As soon as polymer R7 is produced, a strong oxidation reaction occurs to form R8 ($m/z = 62$), which eventually turns into small molecules such as CO_2 , H_2O .

To further clarify the degradation pathways of 2,4-DCP in the GCN-PSFs and GCN, the three-dimensional excitation-emission matrix fluorescence spectra (3D EEMs) was performed [54] (Fig. 7b–e and Fig. S8b–e). As shown in Fig. 7b, there is only one fluorescence center in the whole degradation process, which may belong to 2,4-DCP molecules. In addition, the intensity of the fluorescence signal decreases continuously, and no additional new fluorescence signal appears with the extension of degradation time, confirming that the intermediate products of 2,4-DCP are rapidly degraded into small molecules such as carbon dioxide and water, etc. From the above analysis, a conclusion can be drawn that the constructed GCN-PSFs showed excellent degradation performance for 2,4-DCP.

3.4. Mechanism on the enhanced performance

To reveal the photon-generated charge carriers behavior and light harvesting ability on the H_2O_2 performance and 2,4-DCP degradation efficiency in the constructed GCN-PSFs, the photocurrent response (PCR), electrochemical impedance spectra (EIS) and photoluminescence spectroscopy (PL) were carried out [55,56]. As shown in Fig. 8a, the PCR density of GCN was significantly stronger than that of other catalysts and remained stable after 8 on-off cycles, indicating that GCN is equipped with more efficient and steady carriers separation efficiency [57]. Analogously, Fig. 8b exhibits that GCN owns the smallest arc radius than that of others, revealing that carriers is subjected to small resistance during the transferring process [58]. In the equivalent circuit inserted in Fig. 8b, the charge transfer resistance (R_2) was connected in parallel

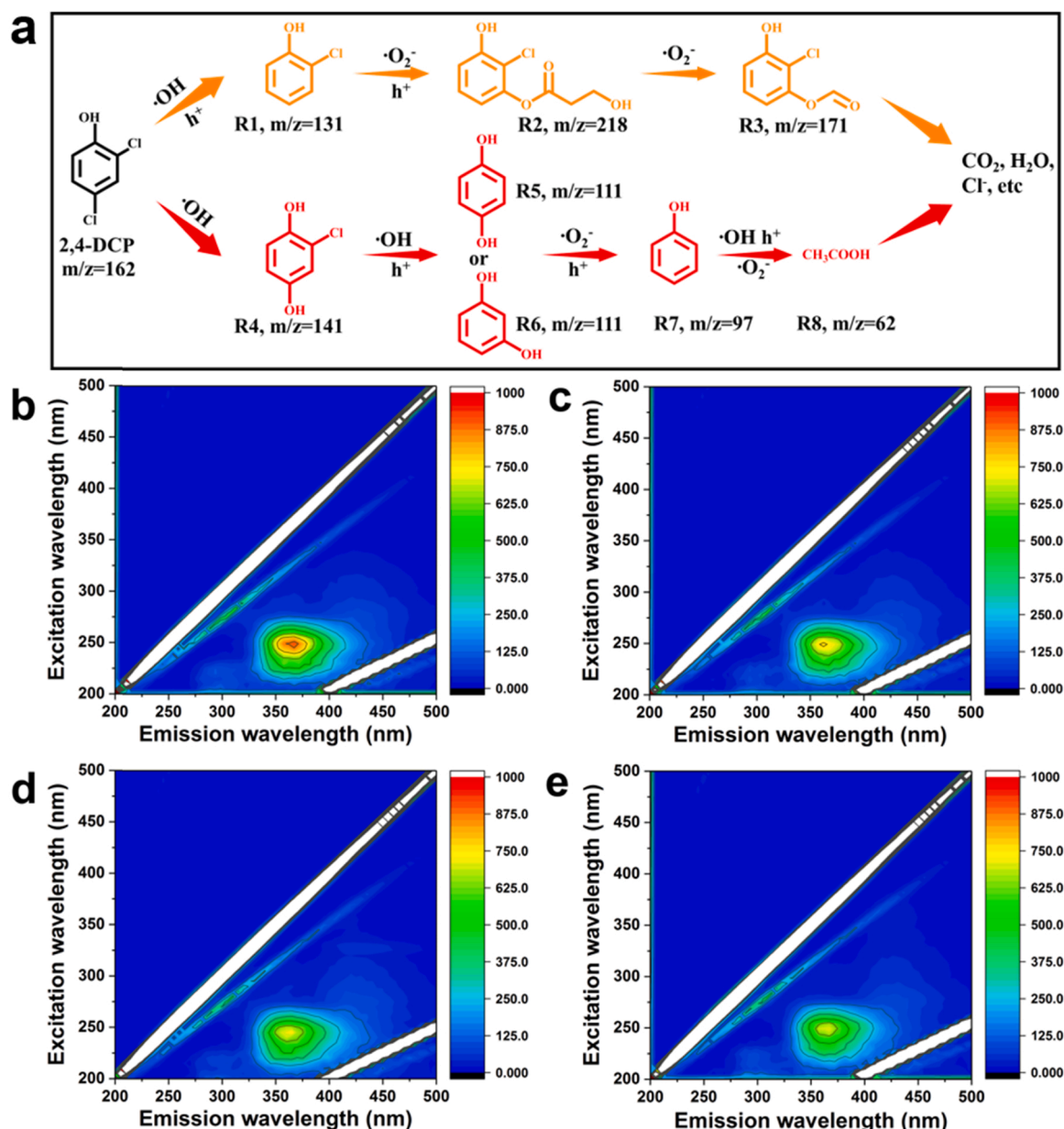


Fig. 7. (a) Presumed 2,4-DCP degradation pathways in GCN-PSFs. (b–e) 3D EEMs of 2,4-DCP solution in GCN-PSFs after visible light irradiation durations of 0 min, 10 min, 20 min and 30 min.

with the constant phase element (CPE1), and then in series with warburg element-open (W1) [59]. The R2 values of all as-prepared samples are illustrated in Table S1, indicating that GCN owned outstanding charge transfer efficiency.

To gain more profound insights into charges recombination and transfer situation, PL was implemented shown in Fig. 8c. Compared with other samples with strong emission peak, the peak strength of GCN with carbon defects decreased dramatically. This phenomenon also confirmed that the carriers in GCN possesses weaker carriers recombination ability [60]. In addition, to explore the role of light absorption capacity of catalyst in the reaction, the UV–vis diffuse reflectance spectroscopy (DRS) was carried out [61,62]. Interestingly, Fig. 8d displays that the absorption wavelength range of GCN is blue shifted, which is attributed to the change of catalyst morphology. The above phenomena is called the quantum limiting effect, which can facilitate the efficient migration of photon-generated carriers to the catalyst surface. Furthermore, according to the Tauc formula [63]:

$$\alpha h\nu = A(h\nu - E_g)^{n/2} \quad (7)$$

the resulting band gap energies (E_g) of BCN and GCN are 2.44 eV and 2.56 eV (Fig. S9). In order to further clarify the band gap structure of BCN and GCN, Mott-Schottky plots was performed (Fig. 8e–f), and the flat band potentials (E_{fb}) of BCN and GCN are -1.17 V and -1.28 V, respectively. The results could be converted into normal hydrogen electrode (NHE) are -0.97 V and -1.08 V. On the basis of previously measured values of E_g and E_{fb} , the valence band (VB) of BCN and GCN were calculated to be 1.47 V and 1.48 V.

To in-depth insight into the mechanism of H_2O_2 generation by $2e^-$ ORR, density functional theory (DFT) calculations were carried out. Fig. 9a–d show the optimized structure of BCN and GCN before and after O_2 adsorption. Obviously, GCN shows more obvious higher adsorption energy of O_2 , demonstrating that the introduction of carbon defects into GCN can dramatically enhance the adsorption capacity of O_2 (Fig. 9e). To further gain insight into the electron transfer in H_2O_2 production

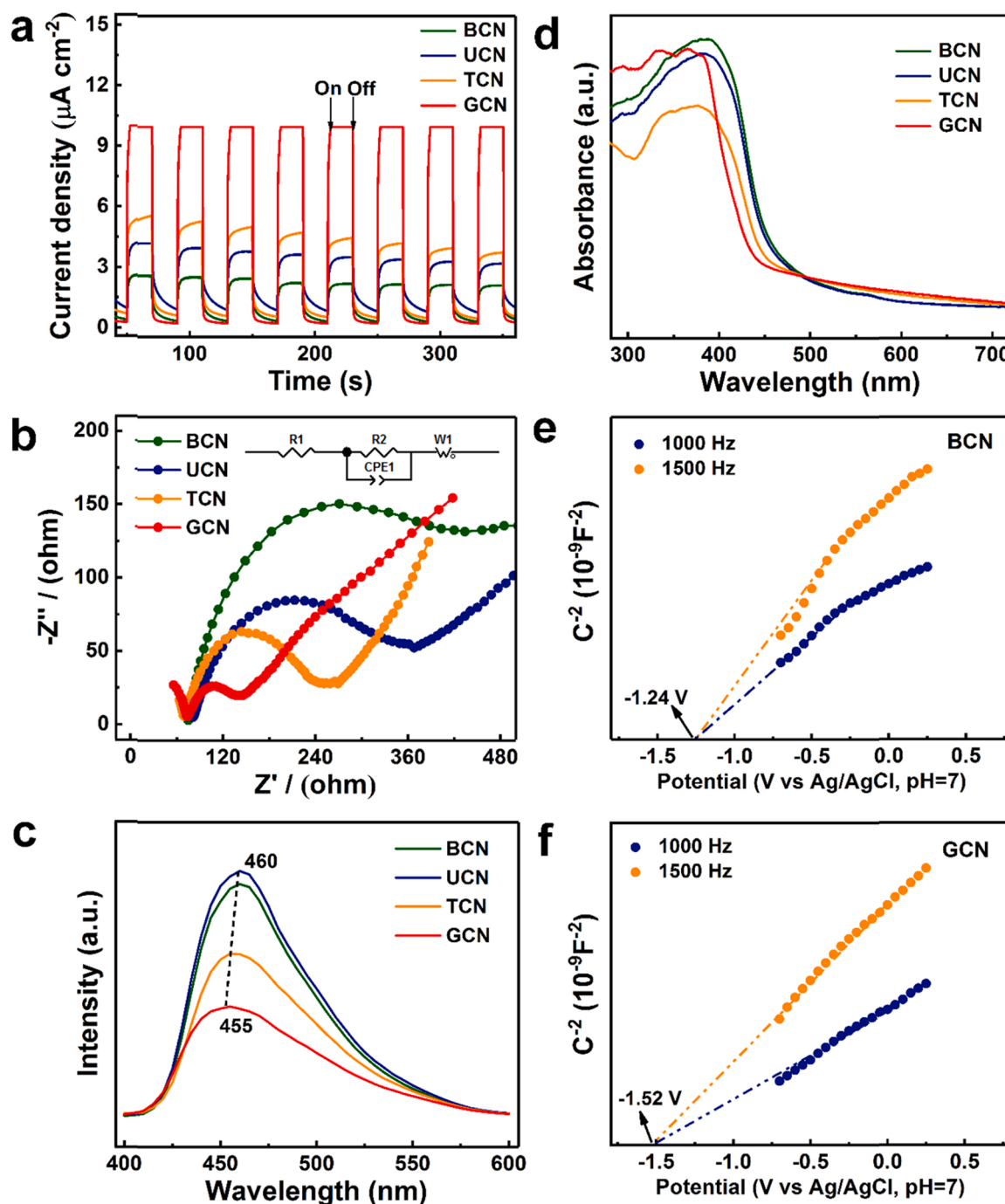


Fig. 8. (a) PCR, (b) EIS, (c) PL and (d) UV-vis DRS of BCN, UCN, TCN and GCN. (e-f) Mott-Schottky plots collected at different frequencies of BCN and GCN.

process, the rotating disk electrode (RDE) of BCN and GCN were performed to obtain the linear sweep voltammetry (LSV) curves which are shown in Fig. S11. The Koutecky-Levich plots is fitted and the average electron transfer number (n) during ORR for BCN and GCN are calculated to be 1.54 and 2.50 (Fig. 9f), implying that GCN is more prone to $2e^-$ ORR to produce H_2O_2 . In addition, based on the analysis of previously measured DRS and Mott-Schottky plots results, electronic band structure of the BCN and GCN were obtained and displayed in Fig. S10. It is noteworthy that the CB of GCN has been shifted up significantly, which is conducive to the $2e^-$ ORR, thus increasing the yield of H_2O_2 . What's more, according to the above results, a possible degradation mechanism of 2,4-DCP is proposed (Fig. 9g). Evidently, the CB of GCN is -1.08 V, which is more negative than $E(\text{O}_2/\text{H}_2\text{O}_2 = 0.68$ V vs. NHE), so

the O_2 adsorbed on the catalyst surface can react with photogenerated electrons to form H_2O_2 [64]. Additionally, the VB (1.48 V) of GCN are negative than $E(\cdot\text{OH}/\text{H}_2\text{O} = 2.68$ V vs. NHE), suggesting that h^+ do not have enough energy to oxidize H_2O to generate $\cdot\text{OH}$ [65]. However, h^+ generated in the system under visible light can oxidize part of the 2,4-DCP into small molecules with simple structures. Moreover, from the results of quench experiments, there exists some $\cdot\text{O}_2^-$ in the GCN-PSFs. This phenomenon is the result of O_2 molecules react with photoexcited electrons, generating $\cdot\text{O}_2^-$ which can also degrade some of the 2,4-DCP. Most importantly, $\cdot\text{OH}$ is the main reactive substance in the degradation of 2,4-DCP process. Therefore, when Fe^{2+} were added to the system, the H_2O_2 produced in the system can react with added Fe^{2+} , generating a large number of $\cdot\text{OH}$. To sum up, photogenerated e^-

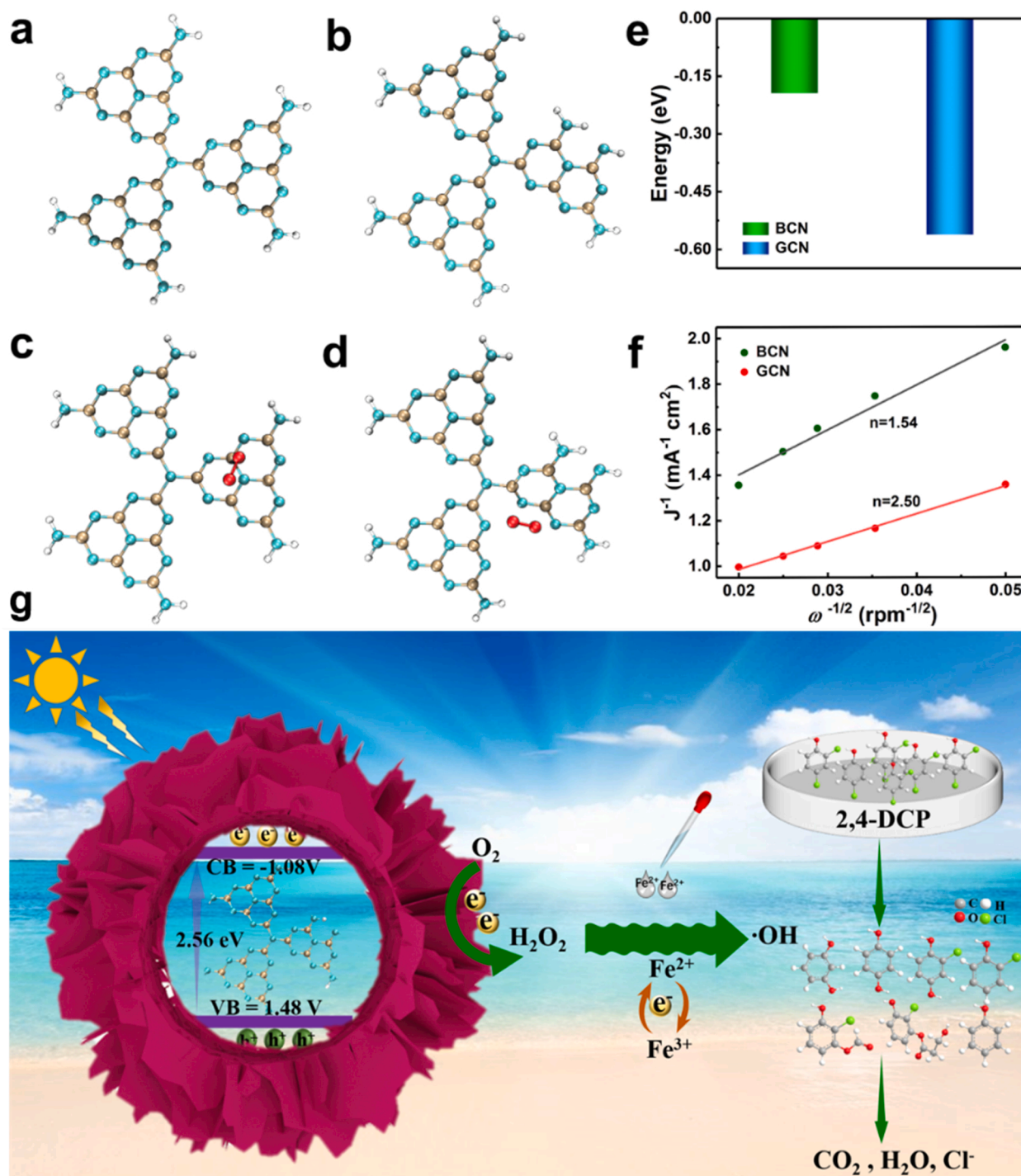


Fig. 9. The optimized structure of (a) BCN and (b) GCN with carbon defects. The structure after O₂ adsorption of (c) BCN and (d) GCN with carbon defects. (e) Adsorption energy of O₂ for BCN and GCN with. (f) Koutecky-Levich plots of the data obtained at the constant electrode potential and the corresponding average number (n) of electrons involved in overall O₂ reduction. (g) Possible degradation mechanism of 2,4-DCP in PSFs.

participated in 2e^- ORR for H_2O_2 production and the Fe^{3+} reduction, thus substantial $\cdot\text{OH}$ radicals were continuously produced through PSFs.

4. Conclusions

In conclusion, different g-C₃N₄-PSFs were constructed on the basis of morphology modulation using melamine as precursor. The GCN with carbon defects exhibits the highest photocatalytic activity for H_2O_2 production ($21.59 \text{ mM h}^{-1} \text{ g}^{-1}$), which is about 5, 3.6 and 2.7 times than that of BCN, UCN and TCN. In addition, the k_{app} value of 2,4-DCP

degradation in GCN-PSFs reaches 0.07 min^{-1} , which is 5.4, 3.3 and 2.6 times higher than that of photocatalysis over BCN, BCN-PSFs and GCN. The introduction of carbon defects in GCN not only accelerates the separation efficiency of charge carriers and increase O₂ adsorption capacity but also improves the 2e^- ORR of H_2O_2 production. Meanwhile, the high-efficient degradation activity of 2,4-DCP in GCN-PSFs is mainly attributed to the in-situ efficient utilization of the H_2O_2 , generating abundant $\cdot\text{OH}$ with strong oxidation. More importantly, GCN-PSFs possesses fine universality and excellent stability. This work advances a new vision for contaminants degradation in Fenton technology, as well

as morphology modulation and defect regulation over g-C₃N₄.

CRediT authorship contribution statement

Yang Wu: Methodology, Software, Validation, Visualization, Writing – original draft. **Juan Chen:** Data curation, Software, Validation, Formal analysis, Writing – review & editing. **Huinan Che:** Validation, Writing – review & editing. **Xin Gao:** Calculation. **Yanhui Ao:** Conceptualization, Writing – review & editing, Supervision, Funding acquisition, Data curation, Validation, Formal analysis. **Peifang Wang:** Writing – review & editing.

Declaration of Competing Interest

The authors declare that they have no known competing financial interests or personal relationships that could have appeared to influence the work reported in this paper.

Acknowledgements

We are grateful for grants from Natural Science Foundation of China (No. 51979081 and No. 52100179), Fundamental Research Funds for the Central Universities (B210202052), National Science Funds for Creative Research Groups of China (No. 51421006), and PAPD.

Appendix A. Supporting information

Supplementary data associated with this article can be found in the online version at doi:10.1016/j.apcatb.2022.121185.

References

- [1] Y. Chen, R. Su, F. Wang, W. Zhou, B. Gao, Q. Yue, Q. Li, In-situ synthesis of CuS@carbon nanocomposites and application in enhanced photo-fenton degradation of 2,4-DCP, *Chemosphere* 270 (2021), 129295.
- [2] X. Gu, J. Mei, J. Lai, S. Lv, J. Yang, S. Cui, S. Chen, Synthesis of Z-Scheme heterojunction ZnNb₂O₆/g-C₃N₄ nanocomposite as a high efficient photo-catalyst for the degradation of 2,4-DCP under simulated sunlight, *Mater. Res. Bull.* 130 (2020), 110939.
- [3] P. He, J. Zhu, Y. Chen, F. Chen, J. Zhu, M. Liu, K. Zhang, M. Gan, Pyrite-activated persulfate for simultaneous 2,4-DCP oxidation and Cr(VI) reduction, *Chem. Eng. J.* 406 (2021), 126758.
- [4] Y. Ma, Y. Gu, D. Jiang, X. Mao, D. Wang, Degradation of 2,4-DCP using persulfate and iron/E-carbon micro-electrolysis coupling system, *J. Hazard. Mater.* 413 (2021), 125381.
- [5] L.S. Zhang, X.H. Jiang, Z.A. Zhong, L. Tian, Q. Sun, Y.T. Cui, X. Lu, J.P. Zou, S. L. Luo, Carbon nitride supported high-loading Fe single-atom catalyst for activating of peroxymonosulfate to generate ¹O₂ with 100% selectivity, *Angew. Chem. Int. Ed.* 60 (40) (2021) 21751–21755.
- [6] Z. Liu, K. Demeestere, S. Hulle, Comparison and performance assessment of ozone-based AOPs in view of trace organic contaminants abatement in water and wastewater: a review, *J. Environ. Chem. Eng.* 9 (2021), 105599.
- [7] M. Sgroi, T. Anumol, F. Vagliasindi, S. Snyder, P. Roccaro, Comparison of the new Cl₂/O₃/UV process with different ozone- and UV-based AOPs for wastewater treatment at pilot scale: removal of pharmaceuticals and changes in fluorescing organic matter, *Sci. Total. Environ.* 765 (2021), 142720.
- [8] J. Ma, K. Wang, C. Wang, X. Chen, W. Zhu, G. Zhu, W. Yao, Y. Zhu, Photocatalysis-self-Fenton system with high-fluent degradation and high mineralization ability, *Appl. Catal. B: Environ.* 276 (2020), 119150.
- [9] W. Wang, H. Xie, G. Li, J. Li, P. Wong, T. An, Visible light-induced marine bacterial inactivation in seawater by an in situ photo-Fenton system without additional oxidants: implications for ballast water sterilization, *ACS E&T Water* 1 (2021) 1483–1494.
- [10] Y. Xu, J. Liu, M. Xie, W. Wei, T. Zhou, J. Yan, H. Xu, H. Ji, H. Li, J. Xie, The construction of a Fenton system to achieve in situ H₂O₂ generation and decomposition for enhanced photocatalytic performance, *Inorg. Chem. Front.* 6 (2019) 1490–1500.
- [11] M. Yalfani, S. Contreras, F. Medina, J. Sueiras, Hydrogen substitutes for the in situ generation of H₂O₂: an application in the Fenton reaction, *J. Hazard. Mater.* 192 (2011) 340–346.
- [12] J. Zhang, G. Zhang, Q. Ji, H. Lan, J. Qu, H. Liu, Carbon nanodot-modified FeOCl for photo-assisted Fenton reaction featuring synergistic in-situ H₂O₂ production and activation, *Appl. Catal. B: Environ.* 266 (2020), 118665.
- [13] T. Fu, X. Gong, J. Guo, Z. Yang, Y. Liu, Zn-CNTs-Cu catalytic in-situ generation of H₂O₂ for efficient catalytic wet peroxide oxidation of high-concentration 4-chlorophenol, *J. Hazard. Mater.* 401 (2021), 123392.
- [14] M. Han, L. Lyu, Y. Huang, J. Liang, M. Xue, T. Wu, J. Li, M. Chen, C. Hu, In situ generation and efficient activation of H₂O₂ for pollutant degradation over CoMoS₂ nanosphere-embedded rGO nanosheets and its interfacial reaction mechanism, *J. Colloid Interface Sci.* 543 (2019) 214–224.
- [15] L. Li, J. Bai, S. Chen, Y. Zhang, J. Li, T. Zhou, J. Wang, X. Guan, B. Zhou, Enhanced O₂ • and HO• via in situ generating H₂O₂ at activated graphite felt cathode for efficient photocatalytic fuel cell, *Chem. Eng. J.* 399 (2020), 125839.
- [16] X. Song, H. Zhang, Z. Bian, H. Wang, In situ electrogeneration and activation of H₂O₂ by atomic Fe catalysts for the efficient removal of chloramphenicol, *J. Hazard. Mater.* 412 (2021), 125162.
- [17] H. Che, X. Gao, J. Chen, J. Hou, Y. Ao, P. Wang, Iodide-induced fragmentation of polymerized hydrophilic carbon nitride for high performance quasi-homogeneous photocatalytic H₂O₂ production, *Angew. Chem. Int. Ed.* 60 (2021) 25546–25550.
- [18] H. Li, S. Xue, Y. Cao, X. Yue, A. Zhang, C. Chen, Photocatalytic reduction of Cr(VI) by WO₃@PVP with elevated conduction band level and improved charge carrier separation property, *Environ. Sci. Ecotechnol.* 3 (2020), 100034.
- [19] Y. Lu, X. Cui, C. Zhao, X. Yang, Highly efficient tandem Z-scheme heterojunctions for visible light-based photocatalytic oxygen evolution reaction, *Water Sci. Eng.* 13 (2020) 299–306.
- [20] X. Wu, H. Ma, W. Zhong, J. Fan, H. Yu, Porous crystalline g-C₃N₄: bifunctional NaHCO₃ template-mediated synthesis and improved photocatalytic H₂-evolution rate, *Appl. Catal. B: Environ.* 271 (2020), 118899.
- [21] R. Chen, J. Chen, H. Che, G. Zhou, Y. Ao, Atomically dispersed main group magnesium on cadmium sulfide as the active site for promoting photocatalytic hydrogen evolution catalysis, *Chin. J. Struct. Chem.* 41 (2022) 2201014–2201018.
- [22] H. Tang, R. Wang, C. Zhao, Z. Chen, X. Yang, D. Bukhvalov, Z. Lin, Q. Liu, Oxamide-modified g-C₃N₄ nanostructures: tailoring surface topography for high-performance visible light photocatalysis, *Chem. Eng. J.* 374 (2019) 1064–1075.
- [23] Y. Chen, J. Li, P. Liao, Y. Zeng, Z. Wang, Z. Liu, Cascaded electron transition in CuWO₄/CdS/CDs heterostructure accelerating charge separation towards enhanced photocatalytic activity, *Chin. Chem. Lett.* 31 (2020) 1516–1519.
- [24] S. Sabhi, J. Kiwi, Degradation of 2, 4-dichlorophenol by immobilized iron catalysts, *Water Res.* 35 (2001) 1994–2002.
- [25] W. Tang, C. Huang, 2, 4-dichlorophenol oxidation kinetics by Fenton's reagent, *Environ. Technol.* 17 (1996) 1371–1378.
- [26] L. Xu, J. Wang, Fenton-like degradation of 2, 4-dichlorophenol using Fe₃O₄ magnetic nanoparticles, *Appl. Catal. B: Environ.* 123 (2012) 117–126.
- [27] Z. Jiang, L. Wang, J. Lei, Y. Liu, J. Zhang, Photo-Fenton degradation of phenol by CdS/rGO/Fe²⁺ at natural pH with in situ-generated H₂O₂, *Appl. Catal. B: Environ.* 241 (2019) 367–374.
- [28] X.X. He, H.Y. Shang, C. Wang, L. Chen, Z. Gong, J. Wang, S.L. Zhao, J. Ma, Significantly influenced photocatalytic performance for H₂O₂ generation over ultrathin g-C₃N₄ through regulating the migration orientation of photogenerated charge carriers, *Chin. Chem. Lett.* 32 (2021) 3377–3381.
- [29] W. Ong, L. Tan, Y. Ng, S. Yong, S. Chai, Graphitic carbon nitride (g-C₃N₄)-based photocatalysts for artificial photosynthesis and environmental remediation: are we a step closer to achieving sustainability? *Chem. Rev.* 116 (2016) 7159–7329.
- [30] F. He, Z. Wang, Y. Li, S. Peng, The nonmetal modulation of composition and morphology of g-C₃N₄-based photocatalysts, *Appl. Catal. B: Environ.* 269 (2020), 118828.
- [31] S. Gao, X. Wang, C. Song, S. Zhou, F. Yang, Y. Kong, Engineering carbon-defects on ultrathin g-C₃N₄ allows one-pot output and dramatically boosts photoredox catalytic activity, *Appl. Catal. B: Environ.* 295 (2021), 120272.
- [32] Z. Zhou, Z. Shen, C. Song, M. Li, H. Li, S. Zhan, Boosting the activation of molecular oxygen and the degradation of tetracycline over high loading Ag single atomic catalyst, *Water Res.* 201 (2021), 117314.
- [33] X. Ma, Y. Lv, J. Xu, Y. Liu, R. Zhang, Y. Zhu, A strategy of enhancing the photoactivity of g-C₃N₄ via doping of nonmetal elements: a first-principles study, *J. Phys. Chem. C* 116 (2012) 23485–23493.
- [34] Y. Zhu, C. Lv, Z. Yin, J. Ren, X. Yang, C. Dong, H. Liu, R. Cai, Y. Huang, W. Theis, S. H. Shen, D.J. Yang, A [001]-oriented hitfor's phosphorus nanorods/polymeric carbon nitride heterostructure for boosting wide-spectrum-responsive photocatalytic hydrogen evolution from pure water, *Angew. Chem. Int. Ed.* 59 (2020) 868–873.
- [35] H. Hou, X. Zeng, X. Zhang, Production of hydrogen peroxide by photocatalytic processes, *Angew. Chem. Int. Ed.* 59 (2020) 17356–17376.
- [36] C. Feng, L. Tang, Y. Deng, J. Wang, Y. Liu, X. Ouyang, H. Yang, J. Yu, J. Wang, A novel sulfur-assisted annealing method of g-C₃N₄ nanosheet compensates for the loss of light absorption with further promoted charge transfer for photocatalytic production of H₂ and H₂O₂, *Appl. Catal. B: Environ.* 281 (2021), 119539.
- [37] H. Zhang, L. Jia, P. Wu, R. Xu, J. He, W. Jiang, Improved H₂O₂ photogeneration by KOH-doped g-C₃N₄ under visible light irradiation due to synergistic effect of defects and K modification, *Appl. Surf. Sci.* 527 (2020), 146584.
- [38] X. Song, N. Li, H. Zhang, L. Wang, Y. Yan, H. Wang, L. Wang, Z. Bian, Graphene-supported single nickel atom catalyst for highly selective and efficient hydrogen peroxide production, *ACS Appl. Mater. Interfaces* 12 (2020) 17519–17527.
- [39] Y. Cui, Z. Ding, P. Liu, M. Antonietti, X. Fu, X. Wang, Metal-free activation of H₂O₂ by g-C₃N₄ under visible light irradiation for the degradation of organic pollutants, *Phys. Chem. Chem. Phys.* 14 (2012) 1455–1462.
- [40] Y. Yang, C. Zhang, D. Huang, G. Zeng, J. Huang, C. Lai, C. Zhou, W. Wang, H. Guo, W. Xue, R. Deng, M. Cheng, W. Xiong, Boron nitride quantum dots decorated ultrathin porous g-C₃N₄: Intensified exciton dissociation and charge transfer for promoting visible-light-driven molecular oxygen activation, *Appl. Catal. B: Environ.* 245 (2019) 87–99.
- [41] W. Wang, Q. Niu, G. Zeng, C. Zhang, D. Huang, B. Shao, C. Zhou, Y. Yang, Y. Liu, H. Guo, W. Xiong, L. Lei, S. Liu, H. Yi, S. Chen, X. Tang, 1D porous tubular g-C₃N₄

- capture black phosphorus quantum dots as 1D/0D metal-free photocatalysts for oxytetracycline hydrochloride degradation and hexavalent chromium reduction, *Appl. Catal. B: Environ.* 273 (2020), 119051.
- [42] M. Frisch, G. Trucks, H. Schlegel, G. Scuseria, M. Robb, J. Cheeseman, G. Scalmani, V. Barone, G. Petersson, H. Nakatsuji, Gaussian 16, Revision C.01, Fox, Gaussian, Inc., Wallingford CT, 2019.
- [43] F. Neese, Software update: the ORCA program system, version 4.0, *Wires Comput. Mol. Sci.* 8 (2017) 73–78.
- [44] T. Lu, F. Chen, Multiwfn: a multifunctional wavefunction analyzer, *J. Comput. Chem.* 33 (2012) 580–592.
- [45] W. Humphrey, A. Dalke, K. Schulten, VMD - visual molecular dynamics, *J. Molec. Graph.* 14.1 (1996) 33–38.
- [46] M. Tang, Y. Ao, C. Wang, P. Wang, Facile synthesis of dual Z-scheme g-C₃N₄/Ag₃PO₄/AgI composite photocatalysts with enhanced performance for the degradation of a typical neonicotinoid pesticide, *Appl. Catal. B: Environ.* 268 (2020), 118395.
- [47] H. Che, C. Li, C. Li, C. Liu, H. Dong, X. Song, Benzoyl isothiocyanate as a precursor to design of ultrathin and high-crystalline g-C₃N₄-based donor–acceptor conjugated copolymers for superior photocatalytic H₂ production, *Chem. Eng. J.* 410 (2021), 127791.
- [48] D. Wang, J. Chen, X. Gao, Y. Ao, P. Wang, Maximizing the utilization of photo-generated electrons and holes of g-C₃N₄ photocatalyst for harmful algae inactivation, *Chem. Eng. J.* 431 (2022), 134105.
- [49] K. Li, J. Chen, Y. Ao, P. Wang, Preparation of a ternary g-C₃N₄-CdS/Bi₄O₅I₂ composite photocatalysts with two charge transfer pathways for efficient degradation of acetaminophen under visible light irradiation, *Sep. Purif. Technol.* 259 (2021), 118177.
- [50] S. Zhou, Y. Wang, K. Zhou, D. Ba, Y. Ao, P. Wang, In-situ construction of Z-scheme g-C₃N₄/WO₃ composite with enhanced visible-light responsive performance for nitenpyram degradation, *Chin. Chem. Lett.* 32 (2021) 2179–2182.
- [51] S. Guo, Y. Tang, Y. Xie, C. Tian, Q. Feng, W. Zhou, B. Jiang, P-doped tubular g-C₃N₄ with surface carbon defects: universal synthesis and enhanced visible-light photocatalytic hydrogen production, *Appl. Catal. B: Environ.* 218 (2017) 664–671.
- [52] C. Cao, J. Wang, X. Yu, Y. Zhang, L. Zhu, Photodegradation of seven bisphenol analogues by Bi₅O₇I/UiO-67 heterojunction: relationship between the chemical structures and removal efficiency, *Appl. Catal. B: Environ.* 277 (2020), 119222.
- [53] X. Gao, J. Chen, H. Che, Y. Ao, P. Wang, Rationally constructing of a novel composite photocatalyst with multi charge transfer channels for highly efficient sulfamethoxazole elimination: mechanism, degradation pathway and DFT calculation, *Chem. Eng. J.* 426 (2021), 131585.
- [54] J. Xu, J. Chen, Y. Ao, P. Wang, 0D/1D AgI/MoO₃ Z-scheme heterojunction photocatalyst: highly efficient visible-light-driven photocatalyst for sulfamethoxazole degradation, *Chin. Chem. Lett.* 32 (2021) 3226–3230.
- [55] R. Mu, Y. Ao, T. Wu, C. Wang, P. Wang, Synergistic effect of molybdenum nitride nanoparticles and nitrogen-doped carbon on enhanced photocatalytic hydrogen evolution performance of CdS nanorods, *J. Alloy. Compd.* 812 (2020), 151990.
- [56] Y. Ao, L. Xu, P. Wang, C. Wang, J. Hou, J. Qian, Preparation of CdS nanoparticle loaded flower-like Bi₂O₃CO₃ heterojunction photocatalysts with enhanced visible light photocatalytic activity, *Dalton Trans.* 44 (2015) 11321–11330.
- [57] R. Jiang, G. Lu, Z. Yan, J. Liu, D. Wu, Y. Wang, Microplastic degradation by hydroxy-rich bismuth oxychloride, *J. Hazard. Mater.* 405 (2021), 124247.
- [58] R. Jiang, G. Lu, M. Wang, T. Dang, J. Liu, Z. Yan, Facet-dependent photoactivity of Mn₃O₄/BiOCl for naproxen detoxication: strengthening effect of Mn valence cycle, *Appl. Catal. B: Environ.* 299 (2021), 120672.
- [59] Y. Wu, Z. Gao, H. Li, X. Sun, D. Li, G. Zhou, H. Cai, X. Wu, Promoting carrier separation efficiently by macroscopic polarization charges and interfacial modulation for photocatalysis, *Chem. Eng. J.* 410 (2021), 128393.
- [60] M. Tang, Y. Ao, P. Wang, C. Wang, All-solid-state Z-scheme WO₃ nanorod/ZnIn₂S₄ composite photocatalysts for the effective degradation of nitenpyram under visible light irradiation, *J. Hazard. Mater.* 387 (2020), 121713.
- [61] J.F. Wang, J. Chen, P.F. Wang, J. Hou, C. Wang, Y.H. Ao, Robust photocatalytic hydrogen evolution over amorphous ruthenium phosphide quantum dots modified g-C₃N₄ nanosheet, *Appl. Catal. B: Environ.* 239 (2018) 578–585.
- [62] G. Huang, W. Ye, C. Lv, D. Butenko, C. Yang, G. Zhang, P. Lu, Y. Xu, S.C. Zhang, H. W. Wang, Y.K. Zhu, D.J. Yang, Hierarchical red phosphorus incorporated TiO₂ hollow sphere heterojunctions toward superior photocatalytic hydrogen production, *J. Mater. Sci. Technol.* 108 (2022) 18–25.
- [63] J. Li, J. Chen, Y. Ao, X. Gao, H. Che, P. Wang, Prominent dual Z-scheme mechanism on phase junction WO₃/CdS for enhanced visible-light-responsive photocatalytic performance on imidacloprid degradation, *Sep. Purif. Technol.* 281 (2022), 119863.
- [64] L. Shi, L. Yang, W. Zhou, Y. Liu, L. Yin, X. Hai, H. Song, J. Ye, Photoassisted construction of holey defective g-C₃N₄ photocatalysts for efficient visible-light-driven H₂O₂ production, *Small* 14 (2018), 1703142.
- [65] L. Yang, G. Dong, D. Jacobs, Y. Wang, L. Zang, C. Wang, Two-channel photocatalytic production of H₂O₂ over g-C₃N₄ nanosheets modified with perylene imides, *J. Catal.* 352 (2017) 274–281.